CASL-U-2015-0095-000

L3:THM.CLS.P11.01 Interim Report:

ITM/DNS for High Volume Fraction Bubbly Flow Regimes, Machine Learning for Closure Support

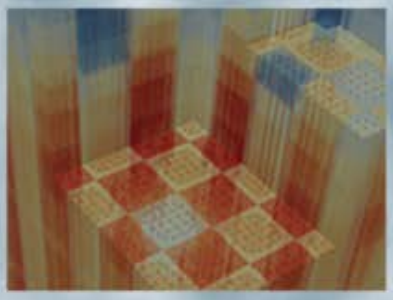

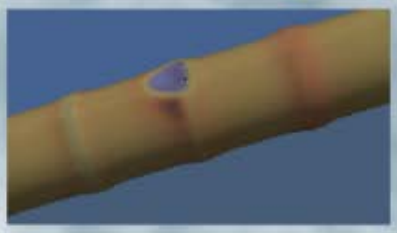

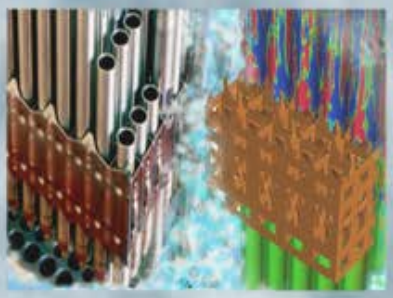

Jun Fang[1]
Igor A. Bolotnov[1]
Jiacai Lu[2]
Gretar Tryggvason[2]

[1]*North Carolina State University*
[2]*University of Notre Dame*

March 31, 2015

CASL-U-2015-0095-000

Interim Report: ITM/DNS for high volume fraction bubbly flow regimes, machine learning for closure support

Progress update for the L3:THM.CLS.P11.01 milestone report

Jun Fang[1]
Igor A. Bolotnov[1]
Jiacai Lu[2]
Gretar Tryggvason[2]

[1]*North Carolina State University*
[2]*University of Notre Dame*

March, 2015

CASL-U-2015-0095-000

Contents

LIST OF FIGURES 3
LIST OF TABLES 3
1. RELEVANCE TO CASL AND OBJECTIVES 4
2. DESCRIPTION OF NUMERICAL CODES 4
3. HIGH VOID FRACTION FLOWS WITH TOPOLOGY CHANGES 4
4. USING DATA MINING FOR CLOSURE OF AVERAGES MODELS 10
4.1. Laminar channel 10
4.2. Turbulent channel 11
5. SINGLE AND TWO-PHASE SUBCHANNEL GEOMETRY SIMULATIONS 14
5.1. Introduction 14
5.2. DNS mesh design 16
5.3. Problem Description 16
5.4. Results and discussion 20
6. BUBBLE-TRACKING CAPABILITIES AND LOCAL FLOW BEHAVIOR ANALYSIS 25
6.1. Local flow analysis 25
6.2 Bubble identification and tracking 25
3.3. Various local parameters 27
3.4 Validation / verification 27
7. LEVEL-SET / FRONT TRACKING SIMULATIONS COMPARISON 29
8. CONCLUSIONS / FUTURE WORK 32

List of Figures

Figure 1. Typical unstructured mesh with boundary layers 17
Figure 2. Wall condition in the subchannel simulations 18
Figure 3. Distribution of 17 bubbles in the turbulent flow (half of the domain can be seen). 19
Figure 4. Distribution of 262 bubbles in the turbulent flow 19
Figure 5. Improved probe design with more reasonable distribution 20
Figure 6. Law of the wall profile for single phase RE01 simulation 21
Figure 7. Law of the wall profile for single phase RE02 simulation 22
Figure 8. Turbulent kinetic energy and dimensionless velocity for single-phase RE01 simulation 22
Figure 9. Turbulent kinetic energy and dimensionless velocity for single phase RE02 simulation 23
Figure 10. Law of the wall profile for two-phase RE01 simulation 24
Figure 11. Turbulent kinetic energy and dimensionless velocity for two phase RE01 simulation 24
Figure 12. Void fraction and gas-liquid velocity profile from two-phase RE01 simulations 25
Figure 13. A slice of the domain of multiple bubble case with marker field shown (zero value indicates liquid) 26
Figure 14. The initial profile of a 262-bubble subchannel case with bubble ID's 26
Figure 15. The steady state velocity profile and marker field of well-controlled bubble within shear rate 2.0 s^{-1}. 28
Figure 16. The steady state velocity profile and marker field of well-controlled bubble within shear rate 10.0 s^{-1}. 28
Figure 17. The bubble relative velocity measured in the flow with shear rate of 2.0 s^{-1} (left) and 10.0 s^{-1}(right). 28
Figure 18. The local shear rate measured in the flow with shear rate of 2.0 s^{-1} (left) and 10.0 s^{-1} (right) . 29
Figure 19. Simulation domain dimensions and axis orientation. Walls are shown as shaded areas. 30
Figure 20. Multiple bubble turbulent channel flow simulation. 31

List of Tables

Table I. Discretization parameters 17
Table II. Fluid properties used in the simulations 21
Table III. The drag and lift coefficients estimated in uniform shear flows 29
Table 4. Overview of non-dimensional and dimensional quantities for 32 bubble simulation 29
Table 5. Hexahedral mesh parameters used for two-phase turbulent channel flow DNS. 31
Table 6. Bubble size and volume fractions in the two-phase flow simulations. 31

1. Relevance to CASL and Objectives

Description: Mining of the results from very large simulations of complex flows to help with the development of LES-like models (supports L1:4, 11). Data obtained by averaging over the homogeneous directions as well as local filtering will be collected and we will explore the relations between unknown closure terms and quantities that are evolved in large-eddy and two-fluid simulations, using linear and nonlinear data reduction techniques (such as regression and neural networks, or more advanced techniques). Simulations will be carried out both in rectangular and subchannel geometries and the data mined from both simulations compared to assess how the geometry affects the small- and the large-scale statistics.

Simulations of high void fraction bubbly flows where topology changes are an important part of the two-phase flow dynamics, and examination of how to use the results for modeling of such flows (supports L1:15). The tasks include obtaining a better understanding of the importance of how the coalescence is modeled, including in turbulent flows, and apply data analysis methods to extract information for modeling of the average or large scale flows. Exploration of the use of low-resolution simulations as model-free LES for complex flows with topology changes and comparison of the evolution of low-order statistics for the large-scale flow with DNS results.

2. Description of numerical codes

This is a joint milestone which utilizes the Front Tracking code (FTC3D) at UND and Level Set based code (PHASTA) at NCSU. For the details on those codes please refer to previous publications [1, 2] as well as one of our previous CASL milestone reports (e.g. L3:THM.CLS.P6.03 “ITM/DNS database of drag, lift and wall effects, including the effects of void fractions”).

3. High void fraction flows with topology changes

Bubbly flows are some of the best-understood gas-liquid flows, and also lend themselves relatively well to direct numerical simulations. They are therefore a natural starting point for investigations aimed at using DNS data to help build models for the average or large scale flow. However, while bubbly flows are common for low void fractions, at higher void fractions the bubbles can merge and breakup and in some cases the frequency and violence of the topology changes make it difficult to identify individual bubbles. Yet, churn-turbulent gas-liquid flows are encountered in practice and must be modeled in any effort to provide a complete predictive strategy for gas-liquid flows. We have started to examine such situations and last year we examined a few cases where bubbles placed in both laminar and turbulent flows

merged to form either large ellipsoidal bubbles or Taylor bubbles, depending on the void fraction. This year the focus is on more complex flows where both merging and breakup takes place.

To examine the evolution we have conducted a series of simulations where all parameters have been kept constant except the surface tension (or the Eötvos number). The initial conditions consists of forty bubbles in a channel of size $\pi \times 2 \times 0.5\pi$, resulting in a void fraction of 13.58%, initially containing turbulent flow with a shear Reynolds number of 128. The interface separating the gas and the liquid is shown in figure 1 for five different times for four cases. In figure 1(a) the surface tension is 0.08 in computational units, giving a Eötvos number of 0.2, based on the diameter of the initial bubbles. In figure 1(b) the surface tension is 0.01 (Eo=1.6), in figure 1(c) it is 0.004 (Eo=4.0) and 0.002 (Eo=8.0) in figure 1(d). The frames have been selected to give an impression of how the flow evolves and are not evenly spaced in time. In figure (a) and (b) the surface tension is sufficiently high so that the bubbles continuously merge to form larger and larger bubbles, until most of the gas is contained in one large bubble. There are smaller bubbles present in (b), formed during the merger of larger bubbles but those will eventually merge with the large bubble. This evolution is similar to what we have seen in results obtained last year. The evolution for the lower surface tension is very different. In both figures 1(c) and 1(d) the initial bubbles initially merge into larger bubbles but these are deformed significantly by the flow and as they grow larger through continuing coalescence they also start to break up. At the latest time we see a few large bubbles and many smaller bubbles for both cases, but the distribution of bubble sizes are different, with the smallest surface tension resulting in large bubbles that are smaller than the large bubbles for the case in figure 1(b) and small bubbles that are smaller than the small bubbles in figure 1(b). The intermediate stages are also very different with significantly more complex evolution taking place for the smallest surface tension, including the formation of long gas filaments. Although the evidence is still inconclusive, it is tempting to speculate that the long time bubble distribution will generally consist of several large and many small bubbles and that the size difference decreases as surface tension is reduced and increases as surface tension is increased, but the limits being one large bubble for high surface tension and many bubbles of the same size for low surface tension. This is, of course, a very preliminary observation and we are currently examining the evidence further, including how to best quantify the size distribution.

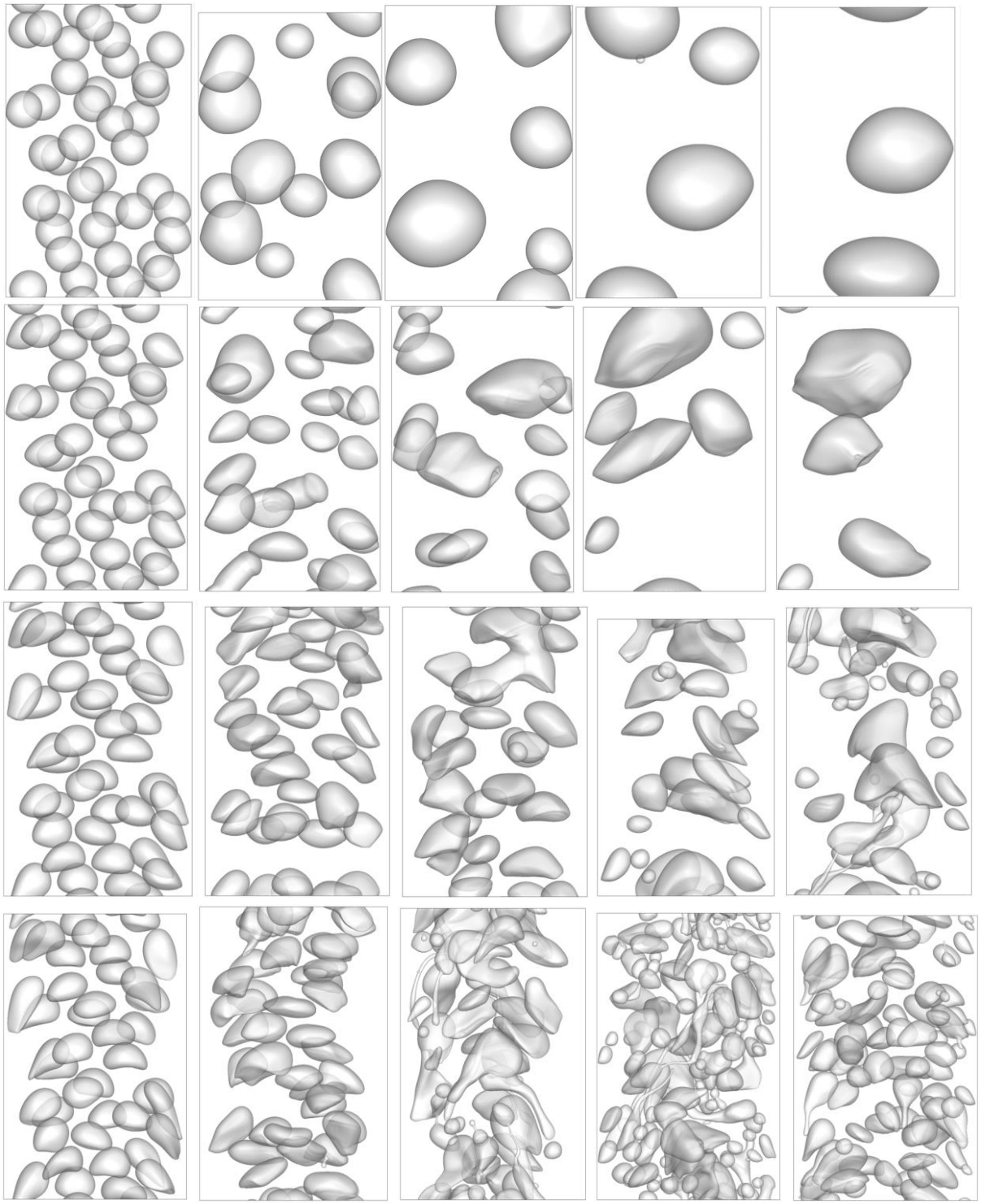

Figure 1. Five frames from four simulations of the evolution of bubbly flows with different surface tension. Frame (a) is on top and frame (d) is on the bottom.

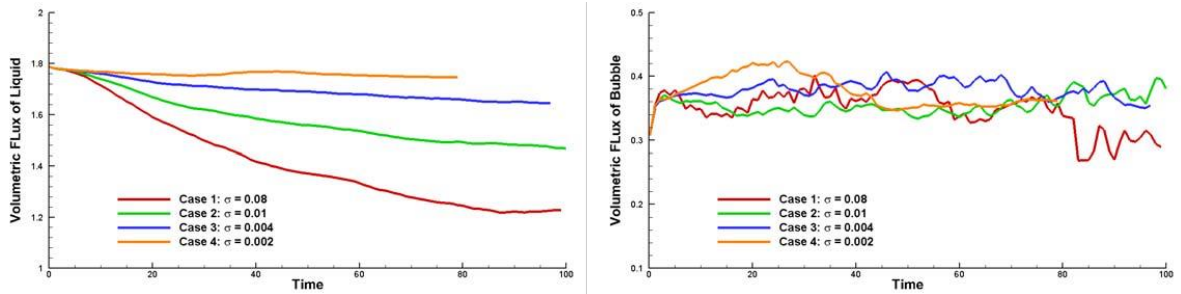

Figure 2. The volumetric flow of liquid for the different cases (left frame) and the volumetric flow of the gas (right frame) versus time.

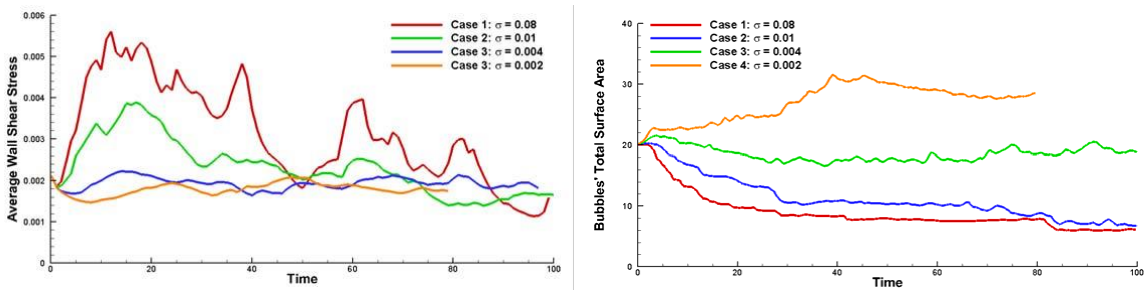

Figure 3. The average wall shear stress (left frame) and the total interface area (right frame) versus time for the different cases.

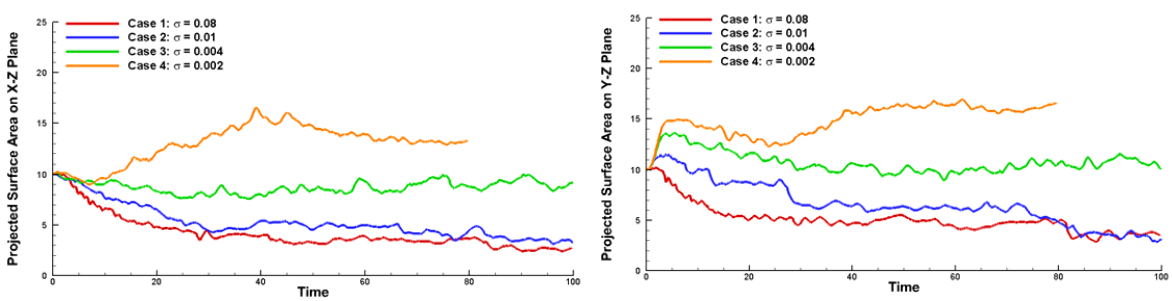

Figure 4. Different projections of the surface area versus time for the different cases.

The evolution of various averaged quantities is shown in figures 2-4. Figure 2 shows the volumetric flow of the liquid and the gas, and it is clear that the flow rate decreases most for the largest surface tension. The average wall shear stress is shown in the left frame of figure 3. Initially, the pressure gradient driving the flow and the weight of the mixture balance the wall shear. As the bubbles are released, the nearly spherical bubbles in the high surface tension cases initially move to the wall and increase the wall shear stress. Their accumulation at the wall does, however, lead to rapid coalescence. The more deformable bubbles for the lower surface tension cases do not move to the wall and the wall shear varies less. As the bubbles in the high surface tension case coalesce they move to the center of the channel and since the bubble becomes ellipsoidal, it tends to block the channel and thus slow down the flow. The lower

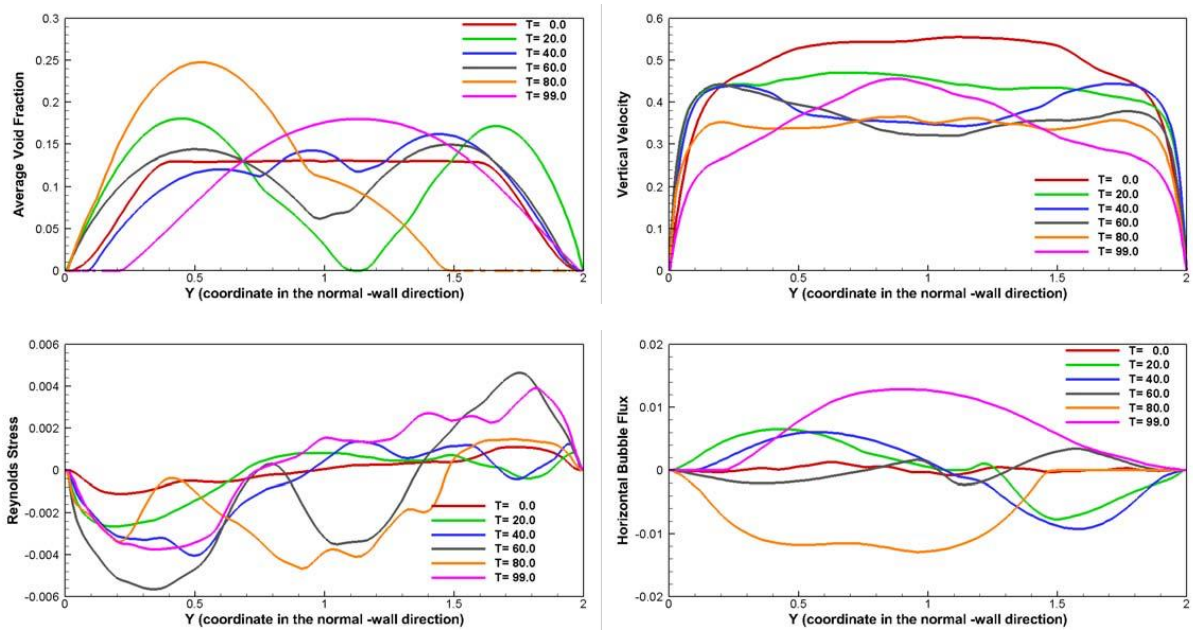

Figure 5. The average void fraction, the average vertical velocity, the streaming stresses and the lateral gas flux at several times for the lowest surface tension case.

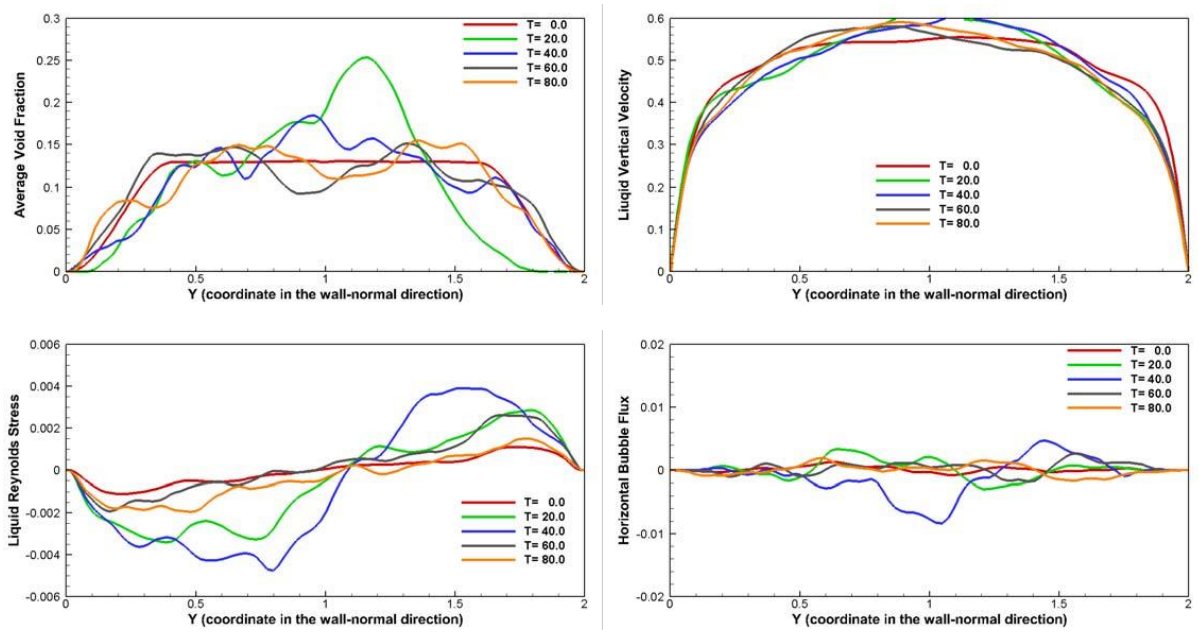

Figure 6. The average void fraction, the average vertical velocity, the streaming stresses and the lateral gas flux at several times for the highest surface tension case.

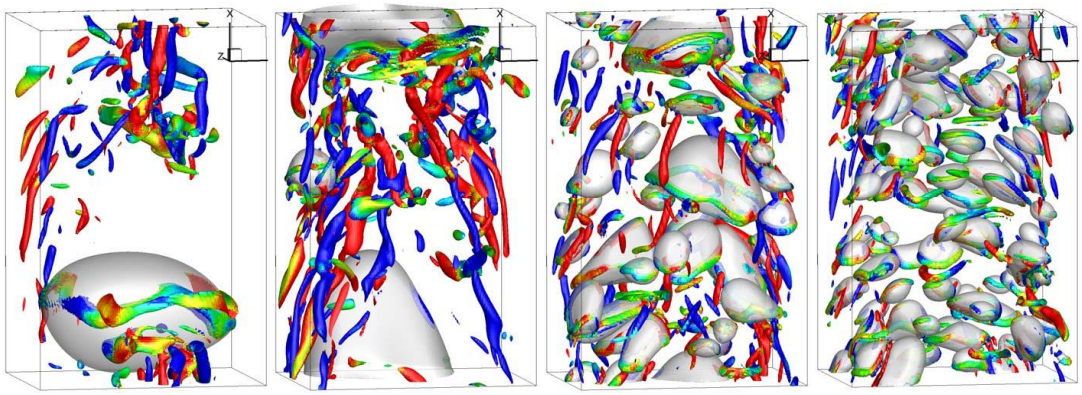

Figure 7. The bubbles and the vortical structures at a late time for all four cases.

surface tension leads to more deformed large bubbles that block the flow less and thus lead to smaller reduction in flow rate. The total surface area is shown in the right frame of figure 3 and here it is clear that for the high surface tension the area decreases as the bubbles merge whereas for the lowest surface tension the breakup increases the surface area. The total surface area only tells us about the average size of the bubbles and in figure 4 we show the projected surface area (or components of the surface area tensor) in two directions. The projected areas start out equal since the bubbles are initially spherical but as they evolve the projected areas diverge as the shape changes.

In addition to overall averaged quantities as shown in figures 2-4, we have also monitored the shape of the various profiles averaged over planes parallel to the walls. Figures 5 and 6 shows an example of this data for two cases (for surface tension equal to 0.08 in figure 5, and for 0.002 in figure 6). The first frame shows the average void fraction and we see that the final void fraction is more peaked in the center for the large surface tension case, as we expect. The second frame shows average vertical liquid velocity and while the velocity changes significantly for the high surface tension, relatively little changes are seen for the low surface tension. The bottom frames show the closure terms needed for the simplest averaged model we are examining. In the lower left corner the streaming stresses are shown and we see that for the lower surface tension these become nearly zero at the latest time for most of the channel, whereas they fluctuate more for the higher surface tension. The lateral gas flux is also very different, becoming essentially zero for the low surface tension and fluctuating more for the high value.

Other quantities that we are monitoring include the structure of the vorticity field and in figure 7 we visualize the vorticity at late time, after the bubbles have coalesced and broken up, for the lower surface tension cases, for all four cases. While the initial velocity field is turbulent, the bubble motion quickly changes the structure of the turbulence in major ways. The vortices are visualized using the lambda-2 method and the color shows their orientation. Red and blue indicate vortices aligned with the flow, but with rotation of the opposite sign and green/yellowish vortices are perpendicular to the flow.

One important question that we started to examine last year but which requires a more thorough study is the details of the coalescence process. The simulations are carried out on a grid with a finite

resolution and even though the flow scales are fully resolved, during the topology change there will always be a time when the diameter of a thin thread or the thickness of a thin film is smaller than the grid spacing. While thin threads snap in realistic ways even if they are not fully resolved, thin films break when they are thin enough for attractive forces to make them unstable. This does, at least in principle, require them to be fully resolved to accurately predict when they rupture. In practice, however, films simulated by methods that advect a marker function directly on a grid rupture in relatively realistic ways, even though they are clearly under-resolved. When the interface between the gas and the liquid it tracked by connected marker points, as we do here, we can control when the merging take place and examine how important the exact timing is. Preliminary studies last year suggested that while the exact time of coalescence does change the detailed evolution, the overall dynamics is not changed.

We will also be examining how we can use the data from the simulations to assist with modeling. For bubbly flows we have had some success with finding the closure terms for a simple two-fluid model by mining the DNS data. The averaged model is derived by averaging over vertical planes parallel to the wall, thus generating time dependent equations that predict the void fraction distribution and the average vertical velocity of the liquid. The model is particularly simple since we neglect the properties of the gas and assume that the vertical gas flux is a function of the instantaneous values of the resolved average variables. For the complex flow examined here we will start with this simple model. However, we expect that the closure terms will not only depend on the resolved average terms but also on variables describing the average state of the unresolved flow.

4. Using data mining for closure of averages models

We have continued to examine both laminar and turbulent channel flows with the goal of developing closure terms for simple two-fluid models and LES-like models. The work on laminar flows is mostly being done by a graduate student funded by an NSF grant, that has somewhat different objectives than the CASL project, but it leverages the CASL study and some of the work has been funded by CASL. The work on turbulent flows is all done under the present project, but has progressed slower, in part because of focus on the complex topology changes discussed in the last section.

4.1. Laminar channel

Our first efforts to use data mining to generate closure terms focused on flows in fully periodic domains with no walls, with non-zero vertical velocity. The initial vertical velocity and the void fraction are specified and depend on only one of the horizontal coordinates. The flow eventually becomes uniform but the transient motion is sensitive to the specific nature of the initial conditions. We derived a simple averaged model for the void fraction and the average vertical velocity as a function of time and one horizontal coordinate. The model contains unknown closure terms, which can be taken to be the lateral gas flux and the liquid streaming stresses. The closure terms can be computed from the DNS results and we use the DNS result to create a database with the closure terms and other averaged quantities. The relationship between the closure terms and the known averaged quantities are then fitted using Neural Networks and the resulting fit used to find the time evolution by solving the average model. The model is then used to simulate different initial conditions, for which we have DNS data, and in all cases do we

find reasonable agreement between the DNS and the mode results. The results have been described in a manuscript submitted for publication (Ma, Lu and Tryggvason, 2015), which acknowledges both NSF and CASL support.

We are currently extending this study to flows in a vertical channel bounded by walls. This requires us to account for the average surface tension as new closure terms. In our original study we left these out, since the bubbles remain nearly spherical, but in wall bounded flows even small deformations, as seen near walls, must be accounted for. The DNS results show that all the bubbles are initially pushed to the walls relatively quickly, the flow then gradually slows down, and eventually some of the bubbles return to the core of the channel, from the wall. While preliminary results for the closure terms are promising and the simple average model accurately predicts the formation of void fraction peaks at the walls, and a reduction in the flow rate, we are still sorting out what the best way is to include the wall effects is.

4.2. Turbulent channel

We have continued a simulation reported on last year where we follow the motion of a large number of bubbles of different sizes in turbulent channel flow. This case was described in some detail in last year's report, but has now been run up to about twice the time reported them. The domain size is $2\pi \times 4 \times \pi$ in the stream-wise, wall normal and span-wise direction, respectively, resolved by $1024 \times 768 \times 512$ grid points and run using 2048 processors on the Titan. The physical parameters are selected such that the Morton number is equal to 5.75×10^{-10} and the void fraction is 0.0304. The bubbles come in four sizes, as listed in Table I. The majority of the bubbles are small and we expect the smallest two sets of bubbles to accumulate at the wall, since our earlier results suggest that the transition between bubbles pushed to the wall and those that are not is around Eo=2.5. The numbers of bubbles for each group were selected so that there are enough small bubbles that can be pushed to the wall to put the core in hydrostatic equilibrium. The properties of the fluid and the bubbles are the same as in our earlier simulations, but the domain size is eight times larger, giving a friction Reynolds number of Re^{+} =500. The bubbles are initially distributed nearly uniformly across the domain but as they start to rise, the smaller bubbles start to migrate toward the walls and form a dense wall-layer. For channels with spherical bubbles, where the lift force pushes the bubbles toward the wall and a bubbly wall-layer is formed, it can be shown that the steady state consists of a wall-layer and a homogeneous core region where the number of bubbles is such that the weight of the mixture balances the imposed pressure gradient. Thus, if the overall void fraction is given, the void fraction in both the core and the wall-layer can be found. Given our experience with the transient evolution of laminar flows, we expect most of the nearly spherical bubbles to initially move to the walls, while the larger deformable ones stay in the middle of the channel (Lu and Tryggvason, 2008).

Number of Bubbles	Diameter of Bubbles	Eotvos Number
4	0.4414	3.805
13	0.3856	2.904
50	0.306	1.829
504	0.16	0.50

Table I. The distribution of bubble sizes for the large run described in this section. The bubble diameter is in computational units.

In figure 8 we show the bubbles at three times, all more advanced than shown last year. The small bubbles are still moving to the walls, although relatively slowly, but the larger bubbles remain in the middle of the channel, for the most part. Figure 9 shows the vorticity (and the bubbles) using the λ_2 method to visualize the vorticity at two times. To understand the vortical structure a little better, we color the vortical structures according to their orientation. Both red and blue vortical structures are aligned with the flow, but red have a positive rotation while the blue ones have a negative rotation. The intermediate colors (light blue, green and yellow) indicate vortical structures that are not aligned with the flow. As expected, the majority of the vortical structures aligned with the flow come in pairs, such that a blue structure is frequently found next to a red one. The frame on the left is at time 64 and several vortices aligned with the flow are visible in the boundary layer. A comparison of this frame with earlier times shows that the coherence of the vorticity next to the walls has been disrupted significantly with the arrival of the small bubbles, although large longitudinal vortices can be seen in regions that are free of bubbles. Relatively coherent vortices aligned with the flow are also seen in the middle of the channel, behind the bubbles. A careful inspection of the figure at the later time (right frame) also shows that the bubbles are not uniformly distributed at the wall but have started to form clusters, leaving some parts of the wall without bubbles.

We have continued to monitor the various averaged quantities, as we reported last year and in figure 10 we show updated plots for a few of those variables. In the top frame we plot the velocity and it is clear that while the velocity has changed very little at time 64, at time 124 it is starting to change. As discussed above, we expect it to be reduced significantly once the flow reaches steady-state. The middle frame shows the void fraction and we see that the void fraction at the wall has exceeded the value predicted by the value predicted for the steady state. This is as we expect, and like what we see in the smaller runs with laminar flow. In the beginning all---or most---of the bubbles move to the wall and only later do they return to the interior of the channel. Finally, in the bottom frame, we show the Reynolds stresses and while only a modest change had taken place at time 64, at the last time larger changes are visible.

A detailed analysis of the data produced by the large run has been slowed down by our focus on flows with topology changes, but we now believe that we have enough data to examine it in more detail, focusing both on averaged two-fluid models as well as LES-like models.

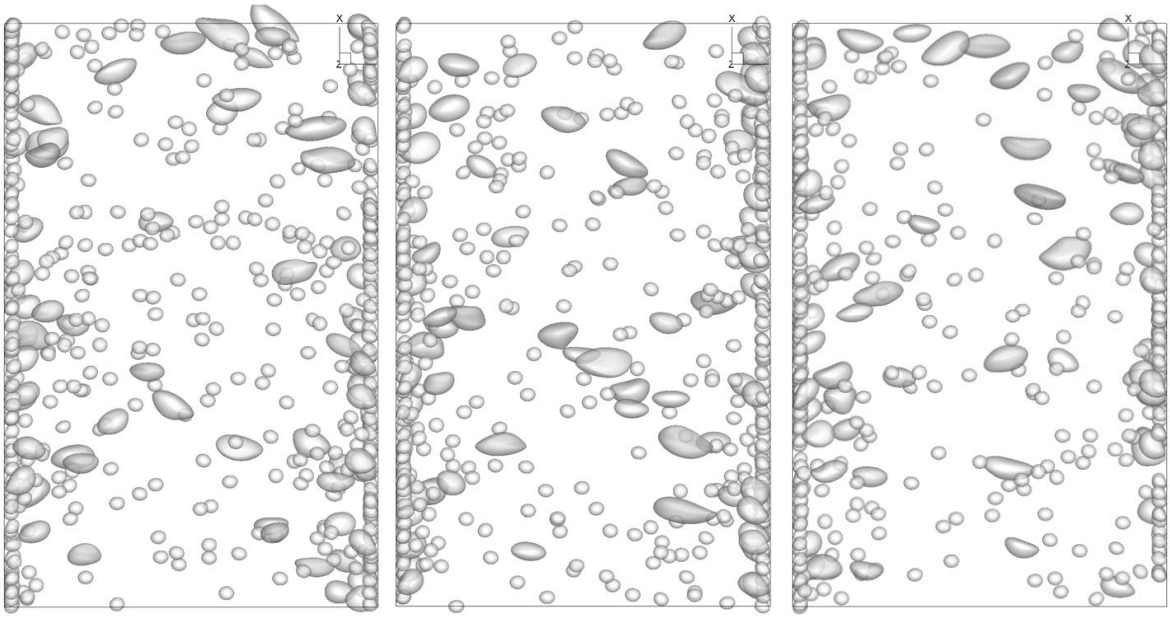

Figure 8. The bubbles at times 78, 94, and 124, as viewed across the channel, parallel to the walls.

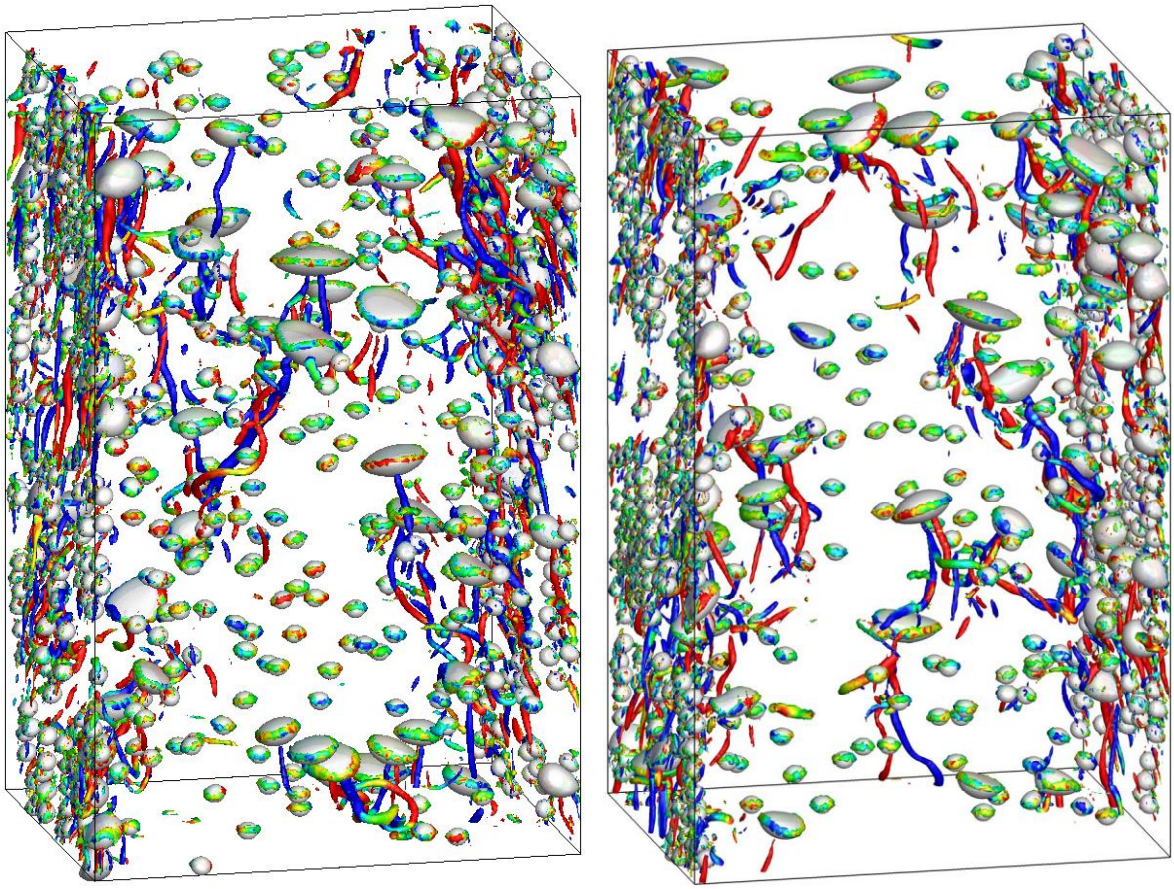

Figure 9. The bubbles and the vertical structures at times 64 (left) and 124 (right).

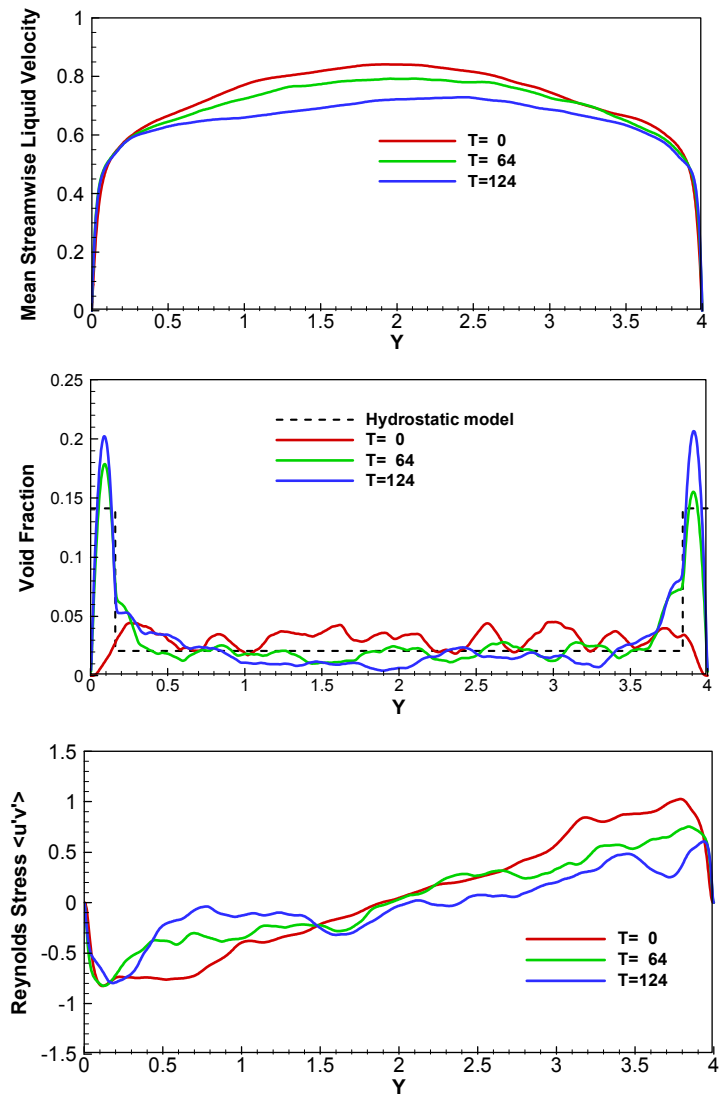

Figure 11. The average velocity (top), the void fraction (middle) and the Reynolds stresses (bottom) for the initial time, time 64, and time 124, versus the wall-normal coordinate.

5. Single and Two-phase Subchannel Geometry Simulations

Note, that this section is based on recently submitted NURETH-16 paper.

5.1. Introduction

A high-fidelity prediction of the single- and two-phase flows in pressurized water reactor (PWR) rod bundles is critical for both reactor safety and thermal-hydraulics analysis. The turbulent flow in the reactor subchannels has been studied for decades both experimentally and computationally. The distributions of axial velocity, turbulence kinetic energy, and Reynolds stress were measured from the experiments of turbulent flows in subchannels of rod bundles in the past with different aspect ratios

(pitch to diameter ratio, P/D) and Reynolds numbers. Trupp and Azad (1975) measured the spatial distributions of mean velocity and Reynolds stresses as functions of Reynolds number and tube spacing for fully developed flow, for which P/D ratios are 1.50, 1.35 and 12, and two Reynolds numbers are used, 12,000 and 84,000 [3]. Carajilescov and Todreas (1976) also did early experiments as well as analytical study to investigate turbulent flows in the subchannel [4]. Detailed experimental data are very important for turbulence modeling and code validation; continued experiments were done by Rehme (1989) [5] and Wu et al. (1993) [6]. The measurement techniques are also being improved over time: Dominguez-Ontiveros and Hassan (2009) have recently done a non-intrusive experimental investigation of flow behavior inside a transparent 5x5 rod bundle with spacer grids using particle image velocimetry (PIV) [7].

Due to the complex and extreme nature of realistic PWR conditions, it is very challenging (if not impossible) and expensive to conduct a full scale real condition experiments to study the turbulent flows in reactor fuel rod bundles. As a result, the computational fluid dynamics (CFD) analysis can be chosen as a practical approach to predict flow behavior in PWR relevant geometries. For instance, the advanced thermal-hydraulic subchannel code COBRA-TF [8] is being used worldwide for best-estimation evaluations of nuclear reactor safety margins. The CFD methodologies are being improved as the nuclear industry advances to generation III+ and generation IV reactor technology. Avramova recently improved the theoretical models and numerics of COBRA-TF [9], and Conner et al. presented the Westinghouse CFD methodology to model single-phase, steady-state conditions in PWR fuel assemblies as well as benchmark testing in [10]. In the meantime, direct numerical simulation (DNS) approach has started to attract the community's attention as a promising tool in studying turbulence phenomena in nuclear reactors due to the rapid development of high performance computing. In DNS of turbulence, the equations of fluid motion (the Navier-Stokes equations) are solved, without turbulence closure assumptions (unlike classic CFD approach), with sufficient temporal and spatial resolution to represent all the scales of turbulence down to Kolmogorov scales [11, 12]. Ninokata and Baglietto have applied DNS to a fully-developed single phase turbulent flow analysis for triangular pin bundles [13, 14], but the Reynolds numbers resolved in their DNS are relatively low (up to Re_h of 24,300).

Besides the single-phase analysis, the study of two-phase turbulence phenomena inside fuel bundles is also of great importance to predict and analyze boiling flows which occur during normal operation and accident conditions in the reactor core. One of the major technological issues in the field of nuclear power is possible departure from nucleate boiling (DNB) condition in the fuel assembly of a nuclear reactor core [15]. The development of new closure laws for computational multiphase fluid dynamics (CMFD) can utilize the detailed information provided by high fidelity interface tracking simulations (ITS) of bubbly flows with DNS of liquid turbulence.

DNS of multiphase flows has been studied previously and provided unprecedented insight into complex flow phenomena. For example, Lu and Tryggvason (2008) studied a turbulent bubbly upflow in a vertical channel using front tracking method, and it is observed that the void fraction profile highly depends on the deformability of the simulated bubbles [2]. Bolotnov et al. also studied the turbulent bubbly flows in flat channels with DNS to investigate the bubble distribution and bubbles' influence on

the turbulence field [1, 16]. Thomas et al. [17, 18] and Fang et al. [19] have implemented a proportional-integral-derivative (PID) controller in ITS to evaluate the drag and lift forces a bubble experiencing in uniform shear flows, and the drag coefficients extracted achieve an excellent agreement with experimentally based correlations [3].

In the presented research, both single and two-phase turbulence are simulated within a PWR subchannel for Reynolds numbers (Re_h) of 29,079 and 80,774 (based on the hydraulic diameter and mean velocity). The turbulent flow of Reynolds number of 29,530 has been previously simulated in a flat channel [1] and will be compared with the case with Re_h of 29,079 to investigate the influence of PWR geometry on the turbulent flow structures. Since the mesh size for DNS grows exponentially as Re_h increases [12], the Reynolds number of 80,774 is chosen as the effort approaching to the simulations with realistic PWR conditions by considering the state-of-the-art computing resources (e.g. currently #5 supercomputer in the world, IBM BG/Q "Mira" at Argonne National Laboratory). Some preliminary results from the low Reynolds number case (29,079) have been presented in [20] from the limited statistical data available at that time, and since then much larger dataset has been collected to help us better understand the bubbly turbulence phenomena in the PWR subchannel. By processing the instantaneous data provided by DNS, statistical results obtained include the mean gas and liquid velocity profiles, void fraction distribution and turbulent kinetic energy profiles. The most novel aspect of current work is that DNS coupled with interface tracking method has been applied to the analysis of turbulent bubbly flows inside the PWR subchannel, which will help develop more accurate closure laws and ensure a higher quality prediction of single and two-phase turbulent flows for nuclear reactor designs.

5.2. DNS mesh design

The following requirements must be met to ensure an accurate representation of all relevant scales in PHASTA simulations: (i) The computational domain must be sufficiently large to contain the largest eddies, and (ii) the grid spacing must be sufficiently fine in order to capture the smaller scales of interest (e.g. Kolmogorov turbulent length scale). The first requirement is met if two-point correlations in the streamwise and spanwise directions vanish within one-half of the computational domain [10]. Meanwhile, the number of mesh points in physical domain must be chosen to resolve the finest scale of appreciable excitation, namely layers of the Kolmogorov dissipation scale thickness [34]. The first plane of grid points off the walls was at a normalized distance of 1.0 (y^+) discussed in [35]. More discussions regarding the DNS resolution requirements for turbulent flows can also be found in [36, 37].

5.3. Problem Description

To create a single PWR subchannel domain, the model is first built in CAD software (SolidWorks), which can be then utilized by meshing tools to generate the corresponding unstructured mesh. Certain number of boundary layers are specified near the fuel rod surface to capture the detailed information regarding the turbulence in the region very close to walls, governed by well-known law of the wall [35]. The mesh size are 53.8 million elements for the case of Re_h of 29,079. Recent progress in advanced parallel meshing tool allows us to generate much larger meshes to fully resolve the turbulence of higher Reynolds numbers, and for the case with Re_h of 80,774 the mesh created includes 1.11 billion elements partitioned into 131,072 parts. Both the domain overview and a zoom-in view for the boundary layers

are illustrated in Figure 1. The length of the subchannel corresponds to about 3 hydraulic diameters (40.5 mm). The cases of two Reynolds numbers are labeled with RE01 (for Re_h of 29,079) and RE02 (for Re_h of 80,774). More detailed discretization parameters are listed in Table I, including domain sizes and resolutions.

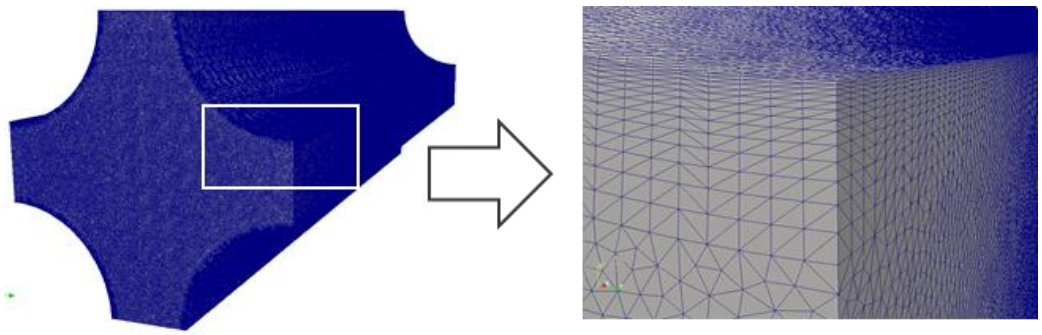

Figure 1. Typical unstructured mesh with boundary layers

Table I. Discretization parameters

Case	RE01	RE02
Domain sizes (mm)	40.5x12.6x12.6	
Rod radius (mm)	4.57	
Reynolds number resolved (Re_h)	29,079	80,774
Bulk resolution (mm)	8.11×10^{-2}	3.25×10^{-2}
Thickness of first B. L. (y^+=1) (mm)	8.11×10^{-3}	3.25×10^{-3}
Number of boundary Layers	13	13
Number of points	9,249,506	186,825,949
Number of elements	53,837,248	1,111,168,768
Number of computing cores used	8,192	131,072
Element per core	6,572	8,478

Periodic boundary conditions are utilized to represent a much longer domain than computationally feasible in DNS approach and to be able to achieve statistically steady state flow conditions. The domain is periodic at inflow and outflow planes as well as the transverse faces, and no-slip wall conditions are applied to the fuel rod surface (Figure 2).

The DNS turbulent results for both single and two-phase flows are produced efficiently using a two-step approach. The single-phase turbulent velocity profile is first generated by placing a sphere blockage region at the domain center to create fluctuations. After large turbulence structures are observed the spherical barrier is removed and the flow can sustain turbulence. The statistical data is

recorded at this point, the convergent behavior is observed as steady state is achieved as shown in Figure 6. When we ensured that the single phase turbulence has achieved statistically steady state flow conditions by comparing averaged velocity profiles over different time windows, the second step was performed to initialize the bubbles (representing a 1% bubble volume fraction), and bubbles' motion and deformation are resolved using level-set interface tracking method. The detailed bubble initialization process has been descripted previously in [20].

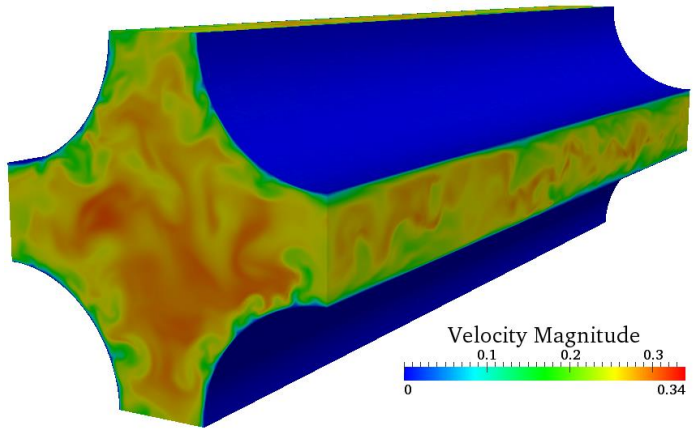

Figure 2. Wall condition in the subchannel simulations

Considering both computational cost and results reliability (based on previous resolution and validation studies) the resolution for bubbles is set to be 20 elements across diameter, which results in 17 bubbles for the 53.8 M mesh and 262 bubbles for the 1.11 B mesh. Higher resolution will result in the rapid increase of computational cost while lower resolution is not capable to capture enough details regarding bubbles' behaviors to reach meaningful conclusions. As shown in Figure 5, a set of virtual probes are designed and placed near outflow plane to record instantaneous velocity fluctuations and bubble distribution across the domain. The bubble distribution and turbulence for 17 bubbles and 262 bubbles are shown in Figure 3 and Figure 4 (the direction of mean flow is from left to right as pointed by the red arrow at bottom-left of figures). Interface tracking simulations are run with the bubbles to allow the flow to fully develop and the bubbles to achieve their terminal velocities.

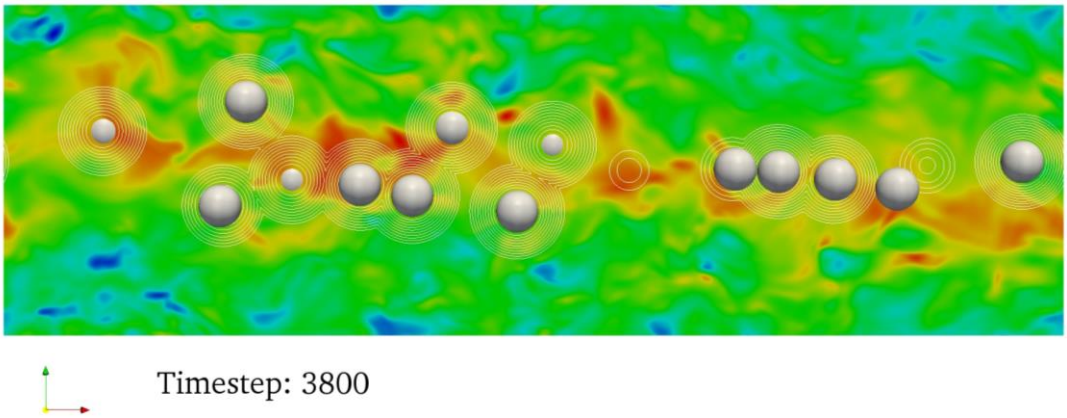

Figure 3. Distribution of 17 bubbles in the turbulent flow (half of the domain can be seen).

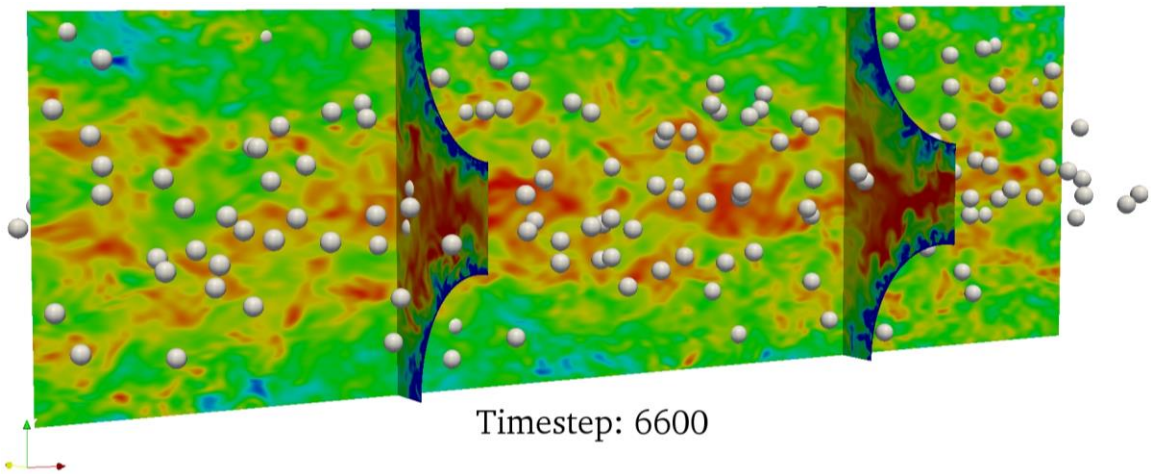

Figure 4. Distribution of 262 bubbles in the turbulent flow

The key computational parameters and fluid properties are listed in Table II. The viscosities and densities of liquid/gas are determined by using the saturated properties of water and vapor at 300 °C. The estimation of realistic PWR conditions can be found in [38]. The data collected from the simulations is processed to obtain, for instance, the mean velocity and turbulent kinetic energy that are calculated based on Eqs. (1) and (2). The probes used to extract the flow statistics are shown in Figure 5 and their location has been improved based on the previous design used in [20]. New probe design is more reasonable, in particular with a much larger distribution density in the boundary layer region in order to capture the flow behavior near the walls.

$$U_i(t) = \frac{1}{N_w}\sum_{j=1}^{N_w} u_i(t + t_j) \tag{1}$$

$$k(t) = \frac{1}{N_w}\sum_{j=1}^{N_w}\sum_{i=1}^{3}\frac{1}{2}u_i'(t+t_j)^2 \tag{2}$$

where, $u_i'(t+t_j) = u_i(t+t_j) - U_i(t)$ is the fluctuation of velocity component-i computed at the time instant $t + t_j$; N_w is the number of velocity samples in each window, t is the current time, $t_j = (j - N_w/2)\Delta t$ is the local window time, and Δt is the time step. For two-phase flows additional parameters, such as void fraction and phasic velocities are also determined using this basic statistical analysis method.

5.4. Results and discussion

Both single- and two-phase subchannel simulations were performed at the Leadership Computing Facility (ALCF) located at the Argonne National Laboratory. The simulation results were visualized using the open-source software, ParaView. Since bubble coalescence can occur with level-set approach when two bubbles are too close from each other, the coalescence control mechanism [39] was introduced in the 17-bubble case to prevent bubbles from coalescing. Generally, two-phase simulations may impose more strict requirements on the flow solver, such as smaller CFL number and larger number of iterations at each timestep. In addition, more simulation time is needed to accurately compute the bubble void fraction distribution for low void fraction flows due to much smaller data available for the gas phase compared to the liquid phase.

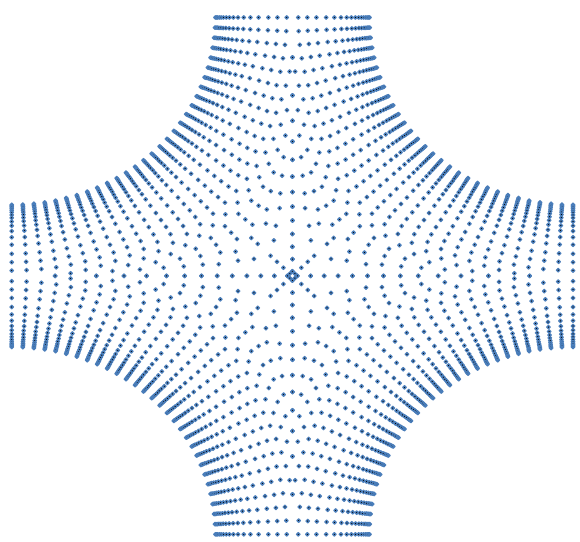

Figure 5. Improved probe design with more reasonable distribution

Table II. Fluid properties used in the simulations

Case	RE01	RE02	Realistic PWR condition
Liquid/Gas Viscosities (Pa·s)	$8.585\text{x}10^{-5}$; $1.965\text{x}10^{-5}$		
Liquid/Gas Densities (kg/m^3)	712.22; 46.17		
Mean velocity (m/s)	0.27	0.75	4.62
Reynolds number (Re_h)	29,079	80,774	452,500

Law of the wall profile shown in Figure 6 with dashed line results in the coefficients of $B = 6.1$ and $\kappa = 0.40$ observed in the single phase RE01 simulations:

$$U^+ = \frac{1}{\kappa}\log y^+ + B \tag{3}$$

These are expected constants for the turbulent law of the wall. We have previously observed the values of $B = 5.5$ and $\kappa = 0.4$ for a rectangular channel which were validated against available data and analytical correlations [40]. Fluctuations in law of the wall measured above are observed for large y^+ (200~400) which does not follow classic flat channel behavior. This behavior is related to the geometry of the subchannel: turbulent flow behavior at the center of subchannel is affected by the four rod walls and thus different from the law of the wall in the boundary layer/rectangular geometry. As shown in Figure 7, the law of the wall analysis for the single-phase RE02 cases leads to the coefficients of $B = 5.4$ and $\kappa = 0.38$. More statistical data is needed to come up with more accurate coefficients.

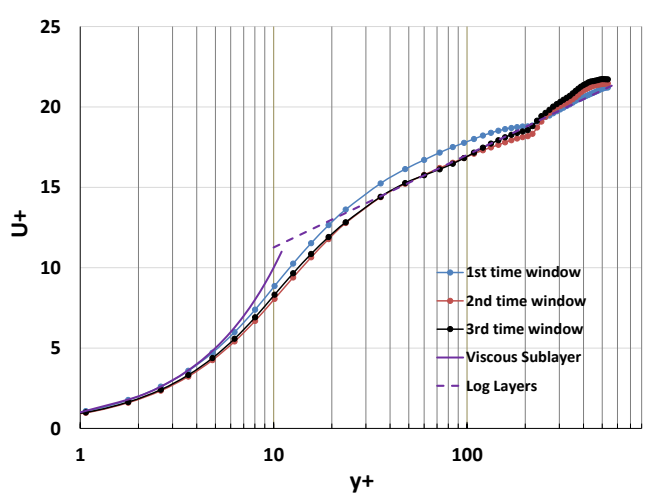

Figure 6. Law of the wall profile for single phase RE01 simulation

The turbulent kinetic energy profile and dimensionless velocity profile are also captured by analyzing the DNS data statistically (Figure 8 and Figure 9). Interestingly, there is a prominent peak on turbulent kinetic energy's decaying tail for RE01 as shown in Figure 8, and distance to the subchannel rod for this inflection is 1.85 mm, which is very close to the half minimum distance between fuel rods (1.71 mm in our cases). As we can see in Figure 5, the probes at the same distance to fuel rod wall can experience different turbulent flow near the center of the subchannel compared to the boundaries. The statistical analysis tools we use are averaging the data from the probes located at a constant distance from the walls to produce each of the point in Figure 8 and Figure 9. At the larger distance from the wall, beyond the minimum half-distance between the fuel rods, the averaging occurs over smaller azimuthal region around each fuel rod. This causes the described behavior at the y+ = 250-300 range shown in Figure 6 for cases RE01. The TKE profile for single phase RE02 is not as smooth as that for single phase RE01 due to the limited statistical data collected for RE02.

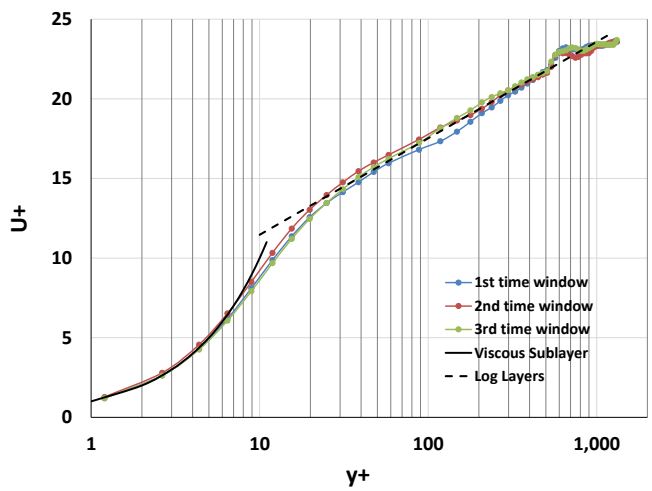

Figure 7. Law of the wall profile for single phase RE02 simulation

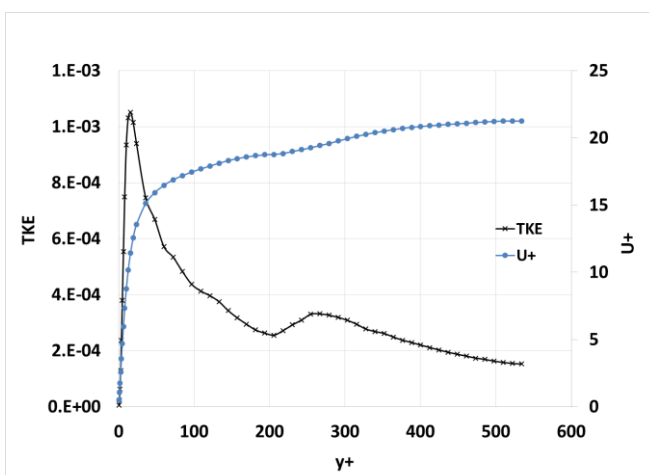

Figure 8. Turbulent kinetic energy and dimensionless velocity for single-phase RE01 simulation

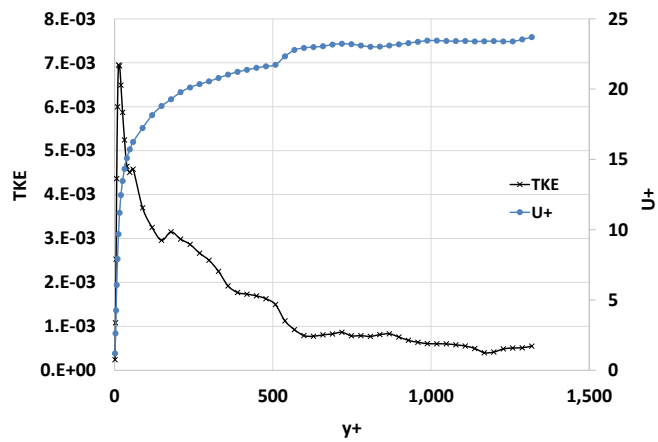

Figure 9. Turbulent kinetic energy and dimensionless velocity for single phase RE02 simulation

Once statistically convergent flow is obtained for the single phase subchannel the bubbles are introduced in the domain through the level set method. The initial condition for the bubbles was specified as the distance field scalar. Seventeen bubbles were initialized in case RE01 and 262 bubbles in case RE02 to represent 1% gas volume fraction two-phase flow (as shown in Figure 3 and Figure 4). We intend to obtain statistically significant data in both cases to analyze the void fraction distribution, as well as gas and liquid mean velocity profiles. Coalescence occurs in the simulations of two-phase RE01, which hinders us from studying the influence of bubbles with a certain size on turbulence in the subchannel. Since the coalescence effects cannot be neglected within the 17-bubble two phase simulations, the coalescence control has been recently developed [37] and is applied to the 17-bubble RE01 simulations. Considering the potential computational cost of coalescence control, the control is not activated in 262-bubble RE02 simulations if the coalescence effect can be mitigated in the case of a large number of bubbles.

As illustrated in Figure 10, Figure 11 and Figure 12, we have statistically processed the recorded data from the two-phase RE01 simulations. However, statistical data available at this moment is limited but will be significantly improved in the final paper version. The distributions shown in in Figure 10, Figure 11 and Figure 12 are extracted from the case in which the bubbles completed just 0.69 flow-throughs. Law of the wall analysis shown in Figure 10 with dashed line results in the coefficients of $B = 8.3$ and $\kappa = 0.55$ observed in the two-phase turbulent subchannel RE01 simulation. The fluctuations observed result from the limited statistics and complex geometry of subchannel. Higher quality statistical results for two-phase RE01 and RE02 simulations are expected to be ready in the following weeks.

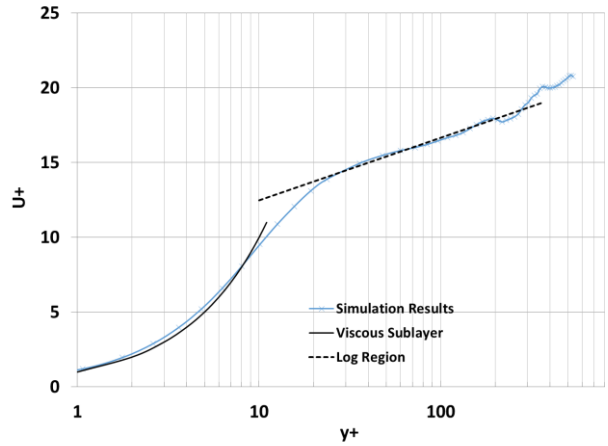

Figure 10. Law of the wall profile for two-phase RE01 simulation

In contrast to the TKE profile in the single-phase RE01 case, the TKE profile of two-phase RE01 case shows a prominent peak which corresponds to the contribution of the bubbles as shown in Figure 11. The distributions of gas and liquid velocity as well as the void fraction from the two-phase RE01 simulations are shown in Figure 12. In the region where the void fraction is higher than 0, the corresponding gas velocity is observed to be larger than liquid velocity because the bubbles are accelerated by the buoyancy force in the subchannel. We would expect this void fraction peak to move closer to the subchannel walls for smaller bubble simulations due to the effect of the lift force. When two-phase flows achieve statistically steady state conditions, the drag coefficient can be estimated based on the bubbly buoyancy force and bubble terminal velocity. By using the steady state assumption and approximating the bubble relative velocity (0.2 m/s), the drag coefficient obtained is 0.498 which is close to the expected value.

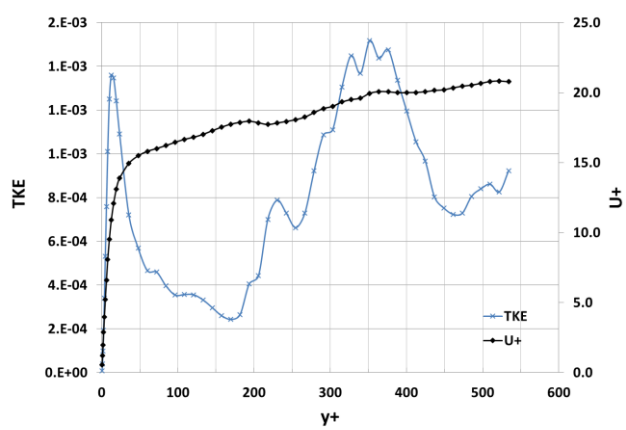

Figure 11. Turbulent kinetic energy and dimensionless velocity for two phase RE01 simulation

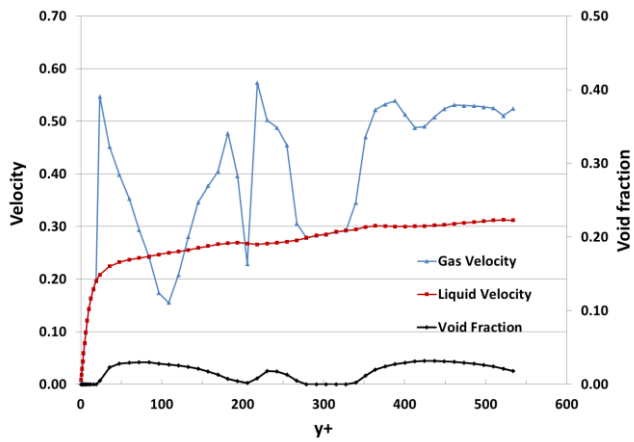

Figure 12. Void fraction and gas-liquid velocity profile from two-phase RE01 simulations

6. Bubble-tracking capabilities and local flow behavior analysis

Note that this section is based on recently submitted paper for Japan/US seminar.

6.1. Local flow analysis

High-fidelity interface tracking simulations with fully resolved liquid behaviors using DNS reveals a new pathway for us to study and understand the bubbly flows. We have gained experience in analyzing the behavior of single bubbles in well controlled conditions. This has been achieved by introducing a PID controller such that the external forces can be adjusted and applied onto a bubble in uniform shear flows to balance off the drag and lift forces. The bubble will be well controlled and stay almost stationary under statistically steady state. By recording the external forces applied, we are able to estimate the corresponding interfacial forces and then calculate the drag/lift coefficients using canonical correlations. Some of the lift and drag estimation results have been presented by Fang et al., (2013) and Thomas et al., (2014). The traditional level-set ITM utilizes a signed distance field to represent two immiscible fluids separated by an interface, which is capable to distinguish different phases (e.g. liquid phase and gas phase). However, it is not capable to identify and track the individual bubbles in the multiple bubble simulations. In the presented work we will demonstrate how the controlled bubble simulations help us verify the algorithms designed to locally analyze the bubble behavior in larger multiple bubble scenarios. Recent progress and preliminary results in development bubble tracking capability for level-set ITM can be found in Fang & Bolotnov, (2014).

6.2 Bubble identification and tracking

In order to identify and track different bubbles, a marker field is created in PHASTA source codes along the level set distance field and every node in the domain has its own marker. The nodes inside the bubbles (or regions of interest) are colored by the corresponding bubble ID while the marker value of a point outside the regions of interest is set to be zero. Figure 13 shows the initial marker field specified for a Cartesian grid. A pre-processing bubble initialization algorithm produces the bubble center

coordinates and the associated ID's, which PHASTA solver is able to read to correctly initialize marker field. As shown in Figure 14, 262 bubbles are initialized with different bubble ID's to represent 1% gas void fraction within the turbulent fluid through a reactor subchannel.

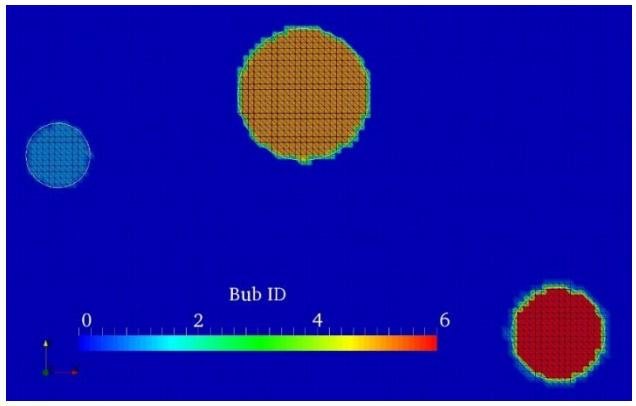

Figure 13. A slice of the domain of multiple bubble case with marker field shown (zero value indicates liquid)

Considering the computational efficiency and simplicity, the marker field is designed to get updated in every timestep based on the level set value and the marker field from the previous timestep. If the point is outside the regions of interest, the corresponding marker value will get reset to be zero. However, when a point is detected to be inside the regions of interest, the code will keep its marker if the old value is non-zero, otherwise, the code will assign the maximum marker from the neighborhood to this point. This simple approach works very well especially when the local Courant number in our two–phase simulations is less than 1.0 (which usually the case). Since PHASTA is a massively parallel code with good scaling performance, the marker field feature has maintained the scaling capabilities and has been tested on large simulations.

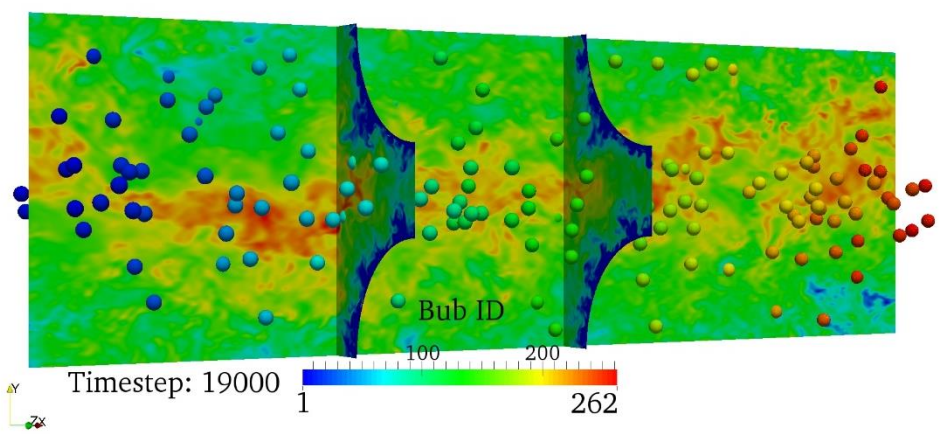

Figure 14. The initial profile of a 262-bubble subchannel case with bubble ID's

3.3. Various local parameters

With the newly developed bubble tracking capability, PHASTA is capable to distinguish and track all the bubbles in the flow and extract various local parameters, including bubble's position, velocity, volume and level of deformation. The average position and velocity of a bubble are averaged among all elements inside the bubble, while the volume can be obtained by integrating the volumes of all bubble elements. To quantify how strongly the bubble is deformed, a deformability factor is introduced as a ratio of the minimum value of level set distance field inside a bubble and the equivalent radius of a sphere that has the same volume as the bubble under consideration ($D = \phi_{min}/R_{eq}$). The deformability factors obtained are consistent with bubbles' deformation over time in test simulations, and the associated uncertainty is observed to be within 10% of expected values. By expanding the regions of interest to cover the local liquid region (shell) near the bubble interface, the code is also capable to collect local liquid parameters, such as local liquid velocity and local liquid shear rate.

Experimental data has always been crucial in the development and validation of multiphase flow models. However, it is very challenging (if not impossible) to measure some quantities in experiments, for instance, the local shear rate in the turbulent bubbly flow experiments. These quantities are very important and can give us valuable insights regarding bubbles' behaviors under different conditions. The bubble tracking capability can be used in large scale DNS coupled with ITM to collect detailed information regarding the individual bubble behavior and correlate it with bubble parameters, which will help develop more accurate closure laws for computational multiphase fluid dynamics and lead to a higher quality prediction of two-phase turbulent flows in current and future generations of nuclear reactor designs.

3.4 Validation / verification

In order to evaluate how well our local analysis approach obtains the parameters of interest it has been decided to test it on two well controlled cases. This way we have full knowledge about the parameters of interest (e.g. relative velocity, shear rate, bubble position) since we utilize small domain and control the bubble.

The two demonstration cases are created and run with both PID controller and bubble tracking capability. A bubble is placed at the domain center in the uniform shear laminar flow with prescribed shear rate of 2.0 s^{-1} and 10.0 s^{-1}. The velocity profiles are defined in such way that the centerline liquid velocity is 0.05 *m/s* in both cases. The thickness of near interface liquid shell for bubble tracking capability is equal to the bubble radius. As expected in Thomas et al., (2015) , the bubble can be successfully controlled in both uniform shear flows (Figure 15 and Figure 16). The recorded information includes magnitude of lift and drag forces, bubble volume, relative velocity as well as local shear rate, based on which the lift and drag coefficients are estimated.

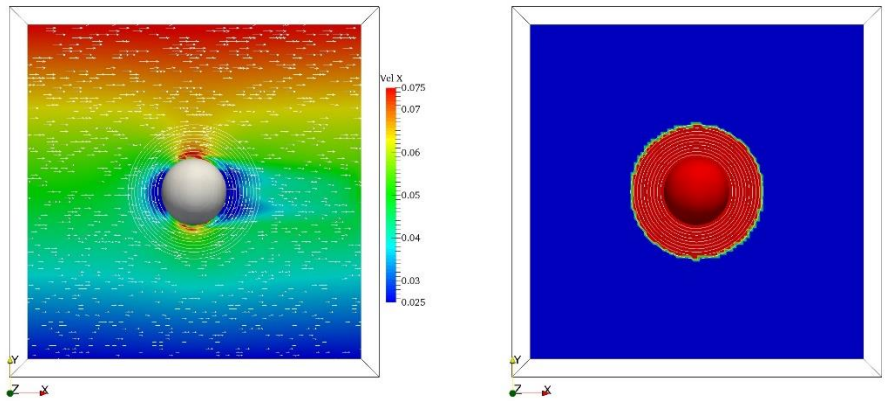

Figure 15. The steady state velocity profile and marker field of well-controlled bubble within shear rate 2.0 s^{-1}.

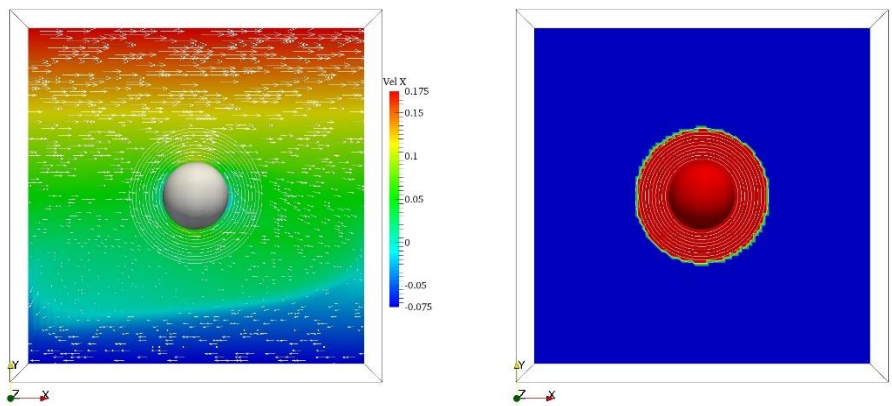

Figure 16. The steady state velocity profile and marker field of well-controlled bubble within shear rate 10.0 s^{-1}.

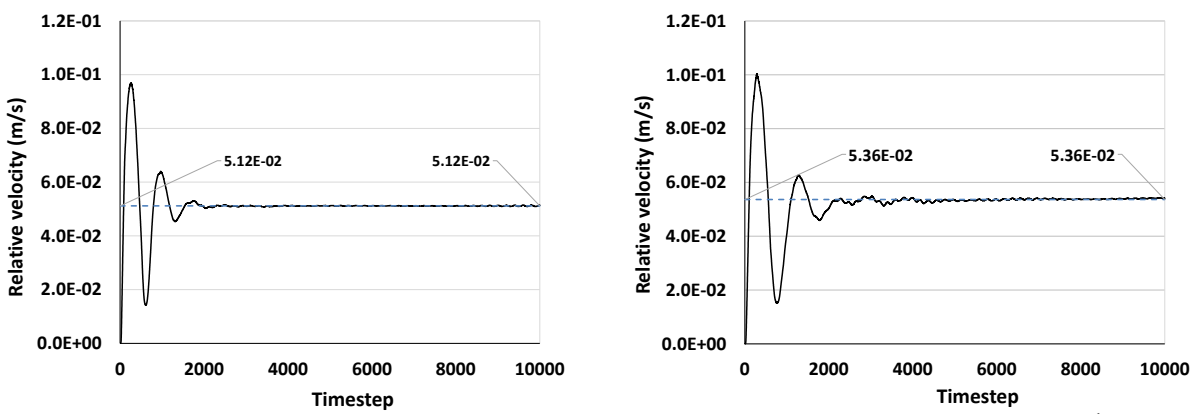

Figure 17. The bubble relative velocity measured in the flow with shear rate of 2.0 s^{-1} (left) and 10.0 s^{-1}(right).

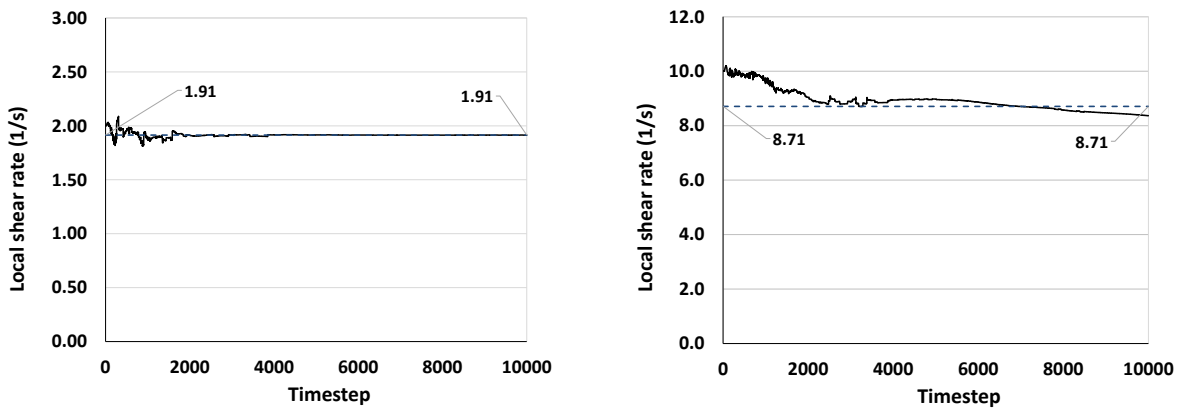

Figure 18. The local shear rate measured in the flow with shear rate of 2.0 s^{-1} (left) and 10.0 s^{-1} (right)

The relative velocity is obtained by averaging the velocity of all liquid elements in the near interface shell, while the local shear rate is estimated by calculating the velocity gradient between top and bottom of liquid shell in y direction. These two quantities are measured in both cases and shown in Figure 18 and Figure 17. Provided the bubble is perfectly controlled and stays stationary, the relative velocity between bubble and the liquid around it is expected to be 0.05 *m/s* which is close to the local liquid velocity extracted (2.32% difference in shear 2.0 s^{-1} and 7.28% difference in shear 10.0 s^{-1}). In the meanwhile, the local shear rates are slightly smaller than the prescribed values. The lift and drag coefficients calculated in both cases are listed in Table III.

Table III. The drag and lift coefficients estimated in uniform shear flows

Shear rate	C_D	C_L
2.0 s^{-1}	0.21	0.51
10.0 s^{-1}	0.25	0.48

7. Level-Set / Front Tracking simulations comparison

As part of this collaboration between UND and NCSU we are planning to perform the same simulation to demonstrate the consistency between the two approaches used to study the bubbly flows. To keep the computational cost reasonable, we have chosen a previously published simulation setup [16]. The details of this simulation are summarized in the following tables and figures.

Table 4. Overview of non-dimensional and dimensional quantities for 32 bubble simulation

Quantity of interest	32 bubble case: non-dimensional value	32 bubble case: dimensional value
Channel width, 2δ	2.0	7.2566 mm
Bubble diameter	0.25	0.9 mm
Liquid superficial velocity	1.1050	0.7114 m/s
Liquid density	1.0	996.5 kg/m^3
Liquid dynamic viscosity	0.00036574	0.0008514 kg/m-s
Reynolds number based on hydraulic diameter	12,085	12,085

Gravity, g	0.08578	9.8 m/s^2
Imposed pressure gradient, ∇p	0.09002	10.2488 kPa/m
Surface tension, σ	0.0487	0.073 kg/s^2
Global Void fraction, <α>	0.01	0.01
Mixture density, ρ_m	0.98831363	984.85 kg/m^3
Gravitational force, $\rho_m g$	0.08478	9.652 kN/m^3
Wall shear	0.00524246	2.1656 N/m^2
Eotvos number	0.110	
Morton number	1.33×10^{-11}	
Weber number	6.268	

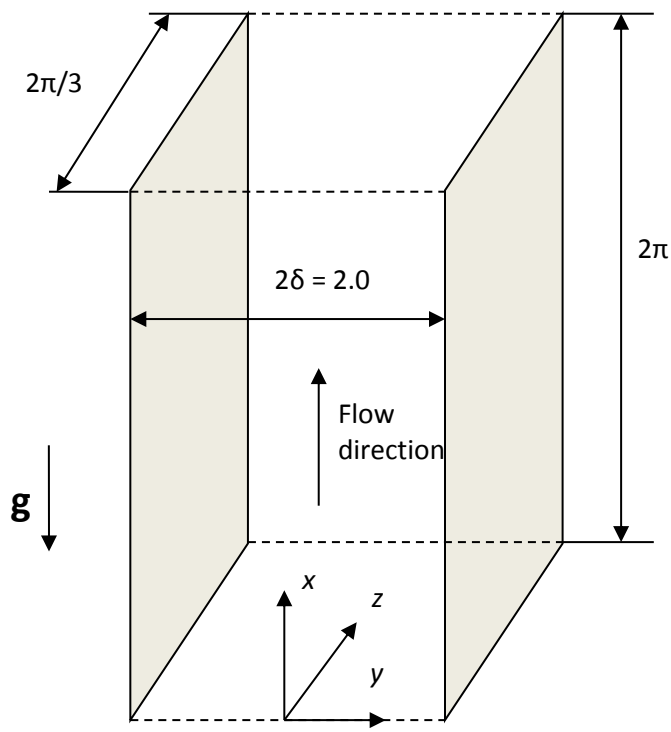

Figure 19. Simulation domain dimensions and axis orientation. Walls are shown as shaded areas.

PHASTA results are shown in Figure 20.

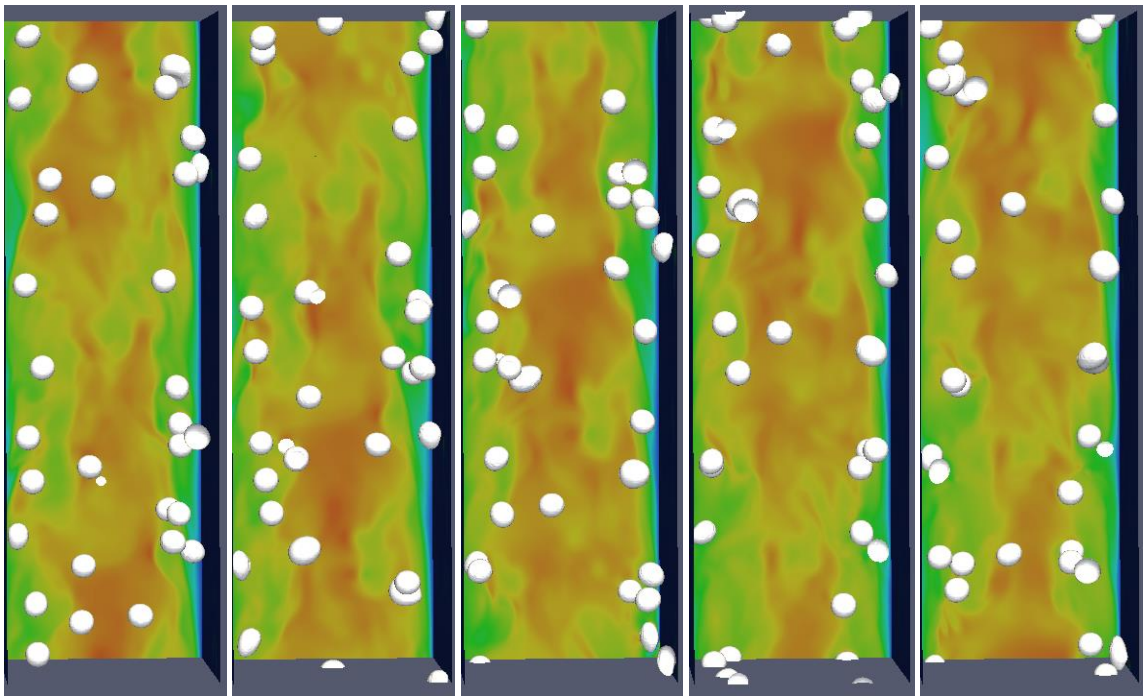

Figure 20. Multiple bubble turbulent channel flow simulation.

Table 5. Hexahedral mesh parameters used for two-phase turbulent channel flow DNS.

Mesh parameters	Stream wise direction, x	Normal to the wall direction, y	Span wise direction, z
Resolution in wall units, Δx_i^+	2.5	2.5	2.5
Number of nodes	452	144	151

Table 6. Bubble size and volume fractions in the two-phase flow simulations.

Bubble diameter (in number of hexahedral elements)	18
Bubble diameter (in wall units)	45
Bubble diameter (in length units)	0.25
Number of bubbles	32
Volume of the bubbles	0.2618
Channel volume	26.319
Bubble volume fraction (i.e., global void fraction)	1.0%

8. Conclusions / Future Work

In the next six months the following work is planned:

- Examine the importance of the coalescence criteria and its influence on the statistics of the flow in more detail.
- Do detailed comparisons between results from front-tracking simulations and PHASTA results for one case.
- Extend the simple two-fluid model used in Ma, Lu and Tryggvason (2015) to the turbulent flow with bubbles of different size and start to assess the relationship of the closure terms to average quantities and summary variables for the unresolved quantities.
- Extend the simple two-fluid model used in Ma, Lu and Tryggvason (2015) to turbulent flows with topology changes and to start to assess the relationship of the closure terms to average quantities and summary variables for the unresolved quantities. It is expected that the closure relationships will be considerably more complex than for bubbly flows and that more exploration of exactly what variables are important needs to be done.
- Apply the local analysis techniques to multiple bubble flows (in pipe, subchannel)
- Develop partitioning methods to recognize the correlated behavior of different bubbles and test this methodology at scale
- Further run the large scale simulations to obtain high quality statistics

References

1. Bolotnov, I. A. “Influence of bubbles on the turbulence anisotropy,” *Journal of Fluids Engineering,* **135**(5), pp. 051301 (2013).

2. Lu, J., & Tryggvason, G. “Effect of bubble deformability in turbulent bubbly upflow in a vertical channel,” *Physics of Fluids (1994-Present),* **20**(4), pp. 040701 (2008).

3. Trupp, A. C., & Azad, R. “The structure of turbulent flow in triangular array rod bundles,” *Nuclear Engineering and Design,* **32**(1), pp. 47-84 (1975).

4. Carajilescov, P., & Todreas, N. “Experimental and analytical study of axial turbulent flows in an interior subchannel of a bare rod bundle,” *Journal of Heat Transfer,* **98**(2), pp. 262-268 (1976).

5. Rehme, K. “Experimental observations of turbulent flow through subchannels of rod bundles,” *Experimental Thermal and Fluid Science,* **2**(3), pp. 341-349 (1989).

6. Wu, X., & Trupp, A. “Experimental study on the unusual turbulence intensity distributions in rod-to-wall gap regions,” *Experimental Thermal and Fluid Science,* **6**(4), pp. 360-370 (1993).

7. Dominguez-Ontiveros, E. E., & Hassan, Y. A. “Non-intrusive experimental investigation of flow behavior inside a 5× 5 rod bundle with spacer grids using PIV and MIR,” *Nuclear Engineering and Design,* **239**(5), pp. 888-898 (2009).

8. Thurgood, M. *COBRA/TRAC, a thermal-hydraulics code for transient analysis of nuclear reactor vessels and primary coolant systems.* The Commission. (1983).

9. Avramova, M. *"Development of an innovative spacer grid model utilizing computational fluid dynamics within a subchannel analysis tool,"* (Ph.D. Dissertation, The Pennsylvania State University). (2007).

10. Conner, M. E., Baglietto, E., & Elmahdi, A. M. "CFD methodology and validation for single-phase flow in PWR fuel assemblies," *Nuclear Engineering and Design,* **240**(9), pp. 2088-2095 (2010).

11. Lee, M., Malaya, N., & Moser, R. D. "Petascale direct numerical simulation of turbulent channel flow on up to 786k cores," Paper presented at the *Proceedings of SC13: International Conference for High Performance Computing, Networking, Storage and Analysis,* pp. 61 (2013).

12. Trofimova, A. V., Tejada-Martínez, A. E., Jansen, K. E., & Lahey Jr, R. T. "Direct numerical simulation of turbulent channel flows using a stabilized finite element method," *Computers & Fluids,* **38**(4), pp. 924-938 (2009).

13. Ninokata, H., Atake, N., Baglietto, E., Misawa, T., & Kano, T. "Direct numerical simulation of turbulent flows in a subchannel of tight lattice fuel pin bundles of nuclear reactors," *Annual Report of the Earth Simulator Center April,* **2005** (2004).

14. Baglietto, E., Ninokata, H., & Misawa, T. "CFD and DNS methodologies development for fuel bundle simulations," *Nuclear Engineering and Design,* **236**(14), pp. 1503-1510 (2006).

15. Anglart, H., & Nylund, O. "CFD application to prediction of void distribution in two-phase bubbly flows in rod bundles," *Nuclear Engineering and Design,* **163**(1), pp. 81-98 (1996).

16. Bolotnov, I. A., Jansen, K. E., Drew, D. A., Oberai, A. A., & Lahey, J. T.,R. "Detached direct numerical simulation of turbulent two-phase bubbly channel flow," *International Journal of Multiphase Flow,* **37**, pp. 647-659 (2011).

17. Thomas, A. M., Fang, J., & Bolotnov, I. A. "Estimation of shear-induced lift force in laminar and turbulent flows," *International Topical Meeting on Advances in Thermal Hydraulics - 2014 (ATH '14),* Reno, NV. (2014).

18. Thomas, A. M., & Bolotnov, I. A. "Evaluating shear induced lift force using interface tracking approach," *Transactions of the 2012 ANS Winter Meeting,* San Diego, CA., Vol. 107, pp. 1277-1278 (2012).

19. Fang, J., Thomas, A. M., & Bolotnov, I. A. "Development of advanced analysis tools for interface tracking simulations," *Transactions of the 2013 ANS Winter Meeting,* Washington D.C., Vol. 109, pp. 1613-1615 (2013).

20. Fang, J., Mishra, A. V., & Bolotnov, I. A. "Interface tracking simulation of two-phase bubbly flow in A PWR subchannel," *International Embedded Topical Meeting on Advances in Thermal Hydraulics - 2014 (ATH '14),* Reno, NV. (2014).